



HAL
open science

Altermagnetic variants in thin films of Mn₅Si₃

Javier Rial, Miina Leiviskä, Gregor Skobjin, Antonín Bad'Ura, Gilles Gaudin, Florian Disdier, Richard Schlitz, Ismaïla Kounta, Sebastian Beckert, Dominik Kriegner, et al.

► **To cite this version:**

Javier Rial, Miina Leiviskä, Gregor Skobjin, Antonín Bad'Ura, Gilles Gaudin, et al.. Altermagnetic variants in thin films of Mn₅Si₃. *Physical Review B*, 2024, 110, pp.L220411. 10.1103/PhysRevB.110.L220411 . hal-04714282v2

HAL Id: hal-04714282

<https://hal.science/hal-04714282v2>

Submitted on 6 Jan 2025


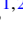
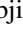



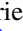





HAL is a multi-disciplinary open access archive for the deposit and dissemination of scientific research documents, whether they are published or not. The documents may come from teaching and research institutions in France or abroad, or from public or private research centers.




L'archive ouverte pluridisciplinaire **HAL**, est destinée au dépôt et à la diffusion de documents scientifiques de niveau recherche, publiés ou non, émanant des établissements d'enseignement et de recherche français ou étrangers, des laboratoires publics ou privés.



Distributed under a Creative Commons Attribution 4.0 International License

Altermagnetic variants in thin films of Mn_5Si_3

Javier Rial ^{1,*}, Miina Leiviskä ^{1,2}, Gregor Skobjin ³, Antonín Bad'ura ^{2,4}, Gilles Gaudin ¹, Florian Disdier,¹
Richard Schlitz ³, Ismaïla Kounta,⁵ Sebastian Beckert ⁶, Dominik Kriegner ², Andy Thomas ^{6,7}, Eva Schmoranzzerová,⁴
Libor Šmejkal,^{2,8} Jairo Sinova,^{8,9} Tomáš Jungwirth ^{2,10}, Lisa Míchez ⁵, Helena Reichlová ²

Sebastian T. B. Goennenwein ³, Olena Gomonay ^{8,†} and Vincent Baltz ^{1,‡}

¹*Univ. Grenoble Alpes, CNRS, CEA, Grenoble INP, IRIG-SPINTEC, F-38000 Grenoble, France*

²*Institute of Physics, Czech Academy of Sciences, Prague, Czechia*

³*Department of Physics, University of Konstanz, Konstanz, Germany*

⁴*Faculty of Mathematics and Physics, Charles University, Prague, Czechia*

⁵*Aix-Marseille Univ., CNRS, CINaM, Marseille, France*

⁶*Institute of Solid State and Materials Physics, TU Dresden, Dresden, Germany*

⁷*Leibniz Institute of Solid State and Materials Science (IFW Dresden), 01069 Dresden, Germany*

⁸*Institute for Physics, Johannes Gutenberg University Mainz, Mainz, Germany*

⁹*Department of Physics, Texas A&M University, College Station, Texas, USA*

¹⁰*School of Physics and Astronomy, University of Nottingham, Nottingham, United Kingdom*



(Received 12 July 2024; revised 15 November 2024; accepted 26 November 2024; published 23 December 2024)

The altermagnet candidate Mn_5Si_3 has attracted wide attention in the context of nonrelativistic spin physics, due to its composition of light elements. In this study, we demonstrate a hallmark of altermagnetism in Mn_5Si_3 thin films, namely the three options, or variants, for the checkerboard distribution of the magnetic Mn atoms. The magnetic symmetries were altered by field-rotation of the Néel vector along relevant crystal directions, resulting in anomalous Hall effect anisotropy. The experimental results in nanoscale devices were corroborated by a theoretical model involving atomic site dependent anisotropy and bulk Dzyaloshinskii-Moriya interaction for a single variant. These findings elevate Mn_5Si_3 from a candidate to a proven altermagnet.

DOI: [10.1103/PhysRevB.110.L220411](https://doi.org/10.1103/PhysRevB.110.L220411)

Altermagnetism has attracted considerable attention, opening up interesting research paths in several fields of condensed matter physics, along with expectations for the emergence of technological applications [1–6]. Altermagnetism features an unconventional combination of favorable characteristics of ferromagnetism and antiferromagnetism [7,8]. An altermagnet presents vanishing net magnetization and can nevertheless feature spin-current effects [9–30]. These originate from the breaking of time-reversal (\mathcal{T}) symmetry, through alternate spin splitting of the energy bands, due to nonrelativistic spin physics [31–40]. \mathcal{T} -symmetry breaking is also naturally manifested in physical tensors, yielding core spintronic properties [9–30] including the anomalous Hall (AHE) [9,10,14,21,24–29] and Nernst (ANE) [11–13] effects. The key factor is that, unlike a conventional antiferromagnet, the magnetic sublattices making up the altermagnet do not have the same environment, linking them by rotational symmetry rather than translation or inversion [1–6]. Seen through the prism of symmetry, crystals of ferromagnets, antiferromagnets, and altermagnets form three distinct groups.

Among the altermagnetic candidates [2,3,25,31,33,41], Mn_5Si_3 is composed of light elements with weak relativistic

spin-orbit coupling, making it possible to link its altermagnetic character to nonrelativistic spin physics [12–14,25–29]. Theoretical predictions [25], alongside the spontaneous AHE [25–27] and ANE [12,13], with influence of crystallinity and Mn content [13,29] despite a weak net magnetization (m), advocates the presence of a d -wave altermagnetic phase. In this phase, Mn_5Si_3 displays a hexagonal cell [25,29]. It is predicted that four Mn atoms on the six possible Mn2 sites exhibit alternating magnetic dipolar ordering, resulting in a checkerboard arrangement of opposite-spin sublattices [Fig. 1(a)]. As there are six possible Mn2 sites, there are three options for the checkerboard distribution of the magnetic atoms. This results in three possible structural domains, or altermagnetic variants, rotated by 120° relative to each other [Fig. 1(a)], and therefore six magnetic domains, when taking into account the Néel vector (n) reversal.

Although theory and experimental evidence advocate the likely altermagnetic phase in thin films of Mn_5Si_3 [12–14,25–29], the specific arrangement of magnetic moments with respect to the crystal environment, i.e., the definitive proof of altermagnetism, remains to be experimentally demonstrated. An only partially successful attempt was made, based on anisotropy of physical properties [27]. More specifically, variation of n with a magnetic field applied at several angles reshuffled the arrangement of the moments with respect to the crystallographic axes, leading to anisotropy in the AHE response [27]. However, the effect of crystalline symmetry

*Contact author: javier.rialrodriguez@cea.fr

†Contact author: ogomonay@uni-mainz.de

‡Contact author: vincent.baltz@cea.fr

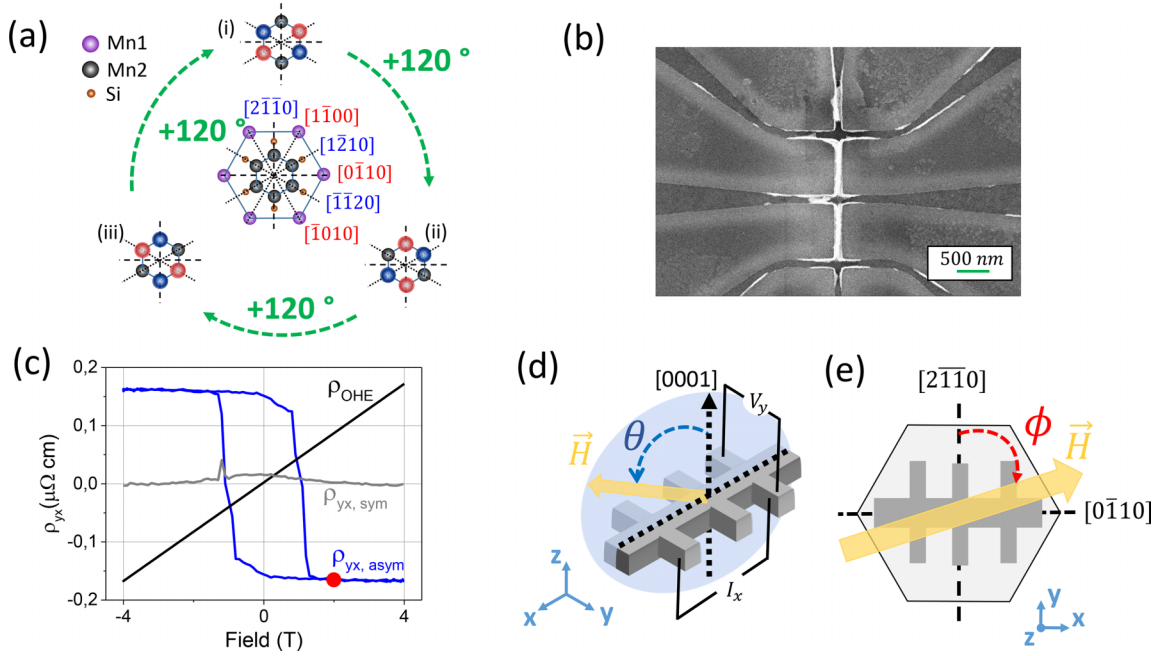


FIG. 1. (a) Hexagonal cell of the Mn_5Si_3 altermagnetic phase, with two magnetically ordered opposite-spin sublattices of Mn2 atoms (red and blue). The variants rotated by 120° are shown. (b) Scanning electron microscopy image of the ~ 100 -nm-wide Hall cross structure used in this work. The white foil is mostly the resist, burned during etching. Redeposition around the corners of the structure cannot be excluded (Fig. S5). (c) Contributions to the field (H) dependence of ρ_{yx} , at $T = 110$ K, for $H \parallel [0001]$. (d), (e) Experimental configurations. θ angle was used for field sweep on a given plane. Plane change was achieved by varying the ϕ angle.

was shown to average out in mesoscopic devices [27], due to the presumed simultaneous presence of all variants [Fig. 1(a)], precluding tracing the sought-after symmetries of Mn_5Si_3 .

In this study, we demonstrate experimentally a hallmark of altermagnetism in Mn_5Si_3 thin films, namely the three options, or variants, for the checkerboard distribution of the magnetically ordered Mn atoms. Our experimental data reveal the symmetries of the system, at the nanoscale, through anisotropy of the AHE for nanometric devices. This finding is corroborated by a theoretical model describing the contributions from \mathbf{n} and \mathbf{m} due to canting, and their field-dependent trajectories, which were inaccessible until now.

A 17-nm-thick epitaxial film of Mn_5Si_3 was grown by molecular beam epitaxy on a 250- μm -thick insulating ($\rho > 10$ k Ω cm) substrate of Si(111). The growth parameters were those optimized in our previous studies [29], to obtain films with the presumed altermagnetic phase [Fig. 1(a)]. A few-nm-thick MnSi phase acted as a priming layer. The film contained 96% Mn_5Si_3 and 4% MnSi, and the epitaxial relationship was Si(111)[$\bar{1}\bar{1}0$]/MnSi(111)[$\bar{2}11$]/ Mn_5Si_3 (0001)[$01\bar{1}0$]. It was patterned into Hall cross structures [Fig. 1(b)], using electron-beam lithography and ion-beam etching. The longitudinal arm was oriented along the $[0\bar{1}10]$ crystalline direction and, consequently, the transverse arms were along $[2\bar{1}\bar{1}0]$. Unless otherwise indicated, the dimension at the intersection of the longitudinal and transverse arms was 100 nm. The current density j_x applied in the longitudinal arm was 5×10^5 A cm^{-2} . The transverse voltage V_y was systematically measured when an external magnetic field H of 2 T, i.e., sufficient to reach saturation out of plane [Fig. 1(c)], was swept in the $(0\bar{1}10)$ and $(\bar{2}110)$ planes and equivalents. Field sweep on a given plane was achieved by varying the θ polar

angle [Fig. 1(d)], and plane change by varying the ϕ azimuthal angle [Fig. 1(e)].

The transverse resistivity ρ_{yx} , deduced from V_y , contains several contributions [25,27], disentangled in a control experiment consisting of varying the H amplitude for a fixed direction: $[0001]$ [Fig. 1(c)]. Those contributions were (1) the linear-in- H ordinary Hall background (ρ_{OHE}), (2) a subsequent negligible symmetric-in- H $\{\rho_{yx,\text{sym}} = [\rho_{yx}(H) + \rho_{yx}(-H)]/2\}$ component, supporting the collinear spin configuration [18], which will be neglected in the rest of the Letter, and (3) the antisymmetric-in- H $\{\rho_{yx,\text{asym}} = [\rho_{yx}(H) - \rho_{yx}(-H)]/2\}$ component, relating to the AHE and corresponding resistivity (ρ_{AHE}) [Figs. S1(a) and S1(b) in the Supplemental Material (SM) [42]]. For all other measurements presented in this work, the θ dependencies of ρ_{yx} were corrected from the expected cosine dependence of the ordinary Hall contribution: $\rho_{\text{AHE}} = \rho_{yx} - \rho_{\text{OHE}} \cos \theta$ [Figs. S1(c) and S1(d)]. Figure 1(c) shows that the H dependence of ρ_{AHE} is in agreement with previous works [25,27] on 10- μm -wide mesoscopic Hall crosses, in terms of both amplitude and coercivity. This finding demonstrates that patterning down to 100-nm-wide Hall crosses leaves the physical properties of the system intact. The kinks observed in ρ_{AHE} , near remanence, are attributed to a gradual rotation of a \mathbf{m} , before switching [Fig. S2(b)]. Note that the measurement temperature used in this work was 110 K, as the films then exhibit the characteristics of an altermagnetic phase, i.e., spontaneous AHE, despite a very low \mathbf{m} of $\sim 0.05\mu_{\text{B}}/\text{u.c.}$ [12,27] [Fig. S2(a)]. Its origin due to the Dzyaloshinskii-Moriya interaction (DMI) will be described later in the text.

Angular(θ) dependencies of $\rho_{\text{AHE}}/\rho_{\text{AHE,max}}$ when \mathbf{H} was rotated in different crystal planes (Fig. 2) allowed us to gain

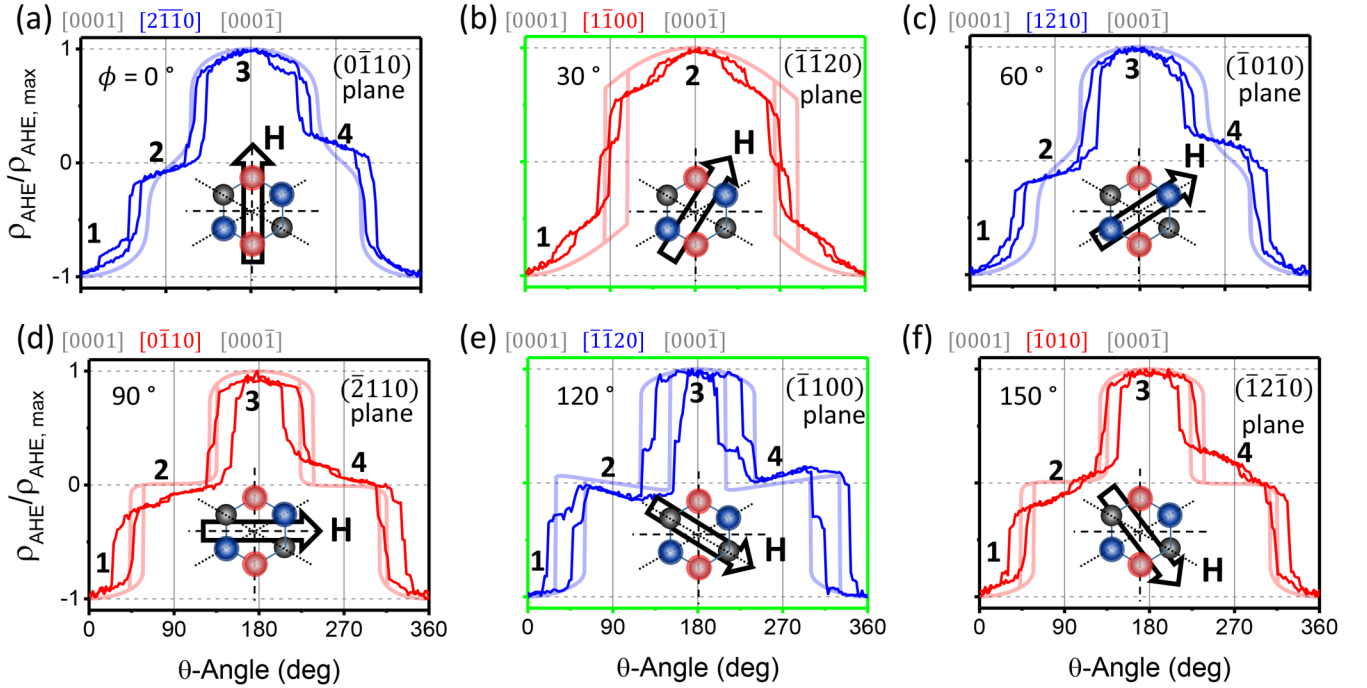


FIG. 2. θ dependence of $\rho_{\text{AHE}}/\rho_{\text{AHE,max}}$, for a ~ 100 -nm-wide Hall cross, when \mathbf{H} of 2 T is rotated in different planes (full lines: experiments; semitransparent: theory). (a), (c), (e) For $\phi = 0, 60, 120^\circ$, \mathbf{H} is rotated in the $(0\bar{1}10)$ plane and equivalent. (b), (d), (f) For $\phi = 30, 90, 150^\circ$, \mathbf{H} is rotated in the $(\bar{2}110)$ plane and equivalent. The majority altermagnetic variant is type (ii) [Fig. 1(a)], as deduced by correlating experiments and theory.

insight into the arrangement of magnetic moments with respect to the crystal axes of Mn_5Si_3 . Based on the presumed symmetry [Fig. 1(a)], data were split into two groups, according to whether \mathbf{H} was rotated: (1) in planes which intercept two Mn2 atoms, i.e., the $(0\bar{1}10)$ plane and its two equivalents $(\bar{1}010)$ and $(\bar{1}100)$ [Figs. 2(a), 2(c), and 2(e)], or (2) in planes which pass between four Mn2 atoms, i.e., the $(\bar{2}110)$ plane and its two equivalents $(1\bar{2}10)$ and $(\bar{1}\bar{1}20)$ [Figs. 2(b), 2(d), and 2(f)]. For all sets of data, $\rho_{\text{AHE}}/\rho_{\text{AHE,max}}$ is maximal when \mathbf{H} is out of plane (for $\theta = 0^\circ$), and flips sign upon \mathbf{H} reversal. This control observation is in line with the field sweep described in Fig. 1(c) and agrees with the \mathcal{T} -symmetry properties of the AHE [25,27]. When \mathbf{H} departs from the out-of-plane direction, all θ dependencies show a multiple steplike behavior, indicating several metastable magnetic configurations. However, the steplike behavior is anisotropic as it depends upon the plane in which \mathbf{H} is rotated. For example, the θ dependence of $\rho_{\text{AHE}}/\rho_{\text{AHE,max}}$ is different when \mathbf{H} is rotated in the $(\bar{1}\bar{1}20)$ plane [Fig. 2(b)], as it exhibits a marked hysteresis around $\theta = 90^\circ$ and 270° , when \mathbf{H} is in plane, as opposed to a plateau for all other configurations [and possibly a tiny hysteresis in Figs. 2(d) and 2(f), which will be commented on later in the text]. These features indicate that there seem to be two metastable states when \mathbf{H} is rotated in the $(\bar{1}\bar{1}20)$ plane, as opposed to four for all other cases. Another significant feature can be seen when \mathbf{H} is rotated in the $(\bar{1}100)$ plane [Fig. 2(e)], in which case the plateau has a negative (positive, respectively) slope around $\theta = 90^\circ$ (270°), in contrast to opposite slopes for all other plateaus.

The steplike anisotropic behaviors, including the marked hysteresis (two stable states)/plateaus (four stable states),

and opposite slopes discussed above for Hall crosses 100 nm wide can be reproduced by a theoretical model (Fig. 2, semitransparent lines). The model is based on the trajectories of the magnetic moments (Fig. 3), when considering a single altermagnetic variant type (ii) [Fig. 1(a)]. It considers a contribution from the Néel vector \mathbf{n} (difference between the sublattice magnetizations) and the net magnetization \mathbf{m} (sum). Their equilibrium orientation under \mathbf{H} is determined by the minimization of the magnetic energy. This energy is introduced on the basis of symmetry considerations. Starting from the crystallographic symmetry of the paramagnetic phase, an additional altermagnetic order parameter [43] describing the local environment of the magnetic Mn2 atoms is introduced (Fig. S6). A DMI-like contribution $H_{\text{DMI}}(n_j m_l + n_l m_j)$ is considered. It originates from the combination of the local environment, formed by five Si and four Mn1 atoms, and deformation (Fig. S7) [25,29]. The subscripts i and j refer to the frame e_j, e_l , which matches the symmetry of any variant [Fig. 1(a)] as follows: e_j connects the two unordered Mn atoms in the basal plane, and e_l points near the $[0001]$ direction. We now focus on variant type (ii), for which e_j is along $[\bar{1}\bar{1}20]$ and e_l points near the $[0001]$ direction, in the $(\bar{1}\bar{1}20)$ plane (Fig. S8). In addition, the local environment imposes the easy magnetic axis along $[\bar{1}\bar{1}20]$. Thus, in the ground state, \mathbf{n} points along $[\bar{1}\bar{1}20]$, which is a C_{2x} symmetry axis for the variant type (ii), and due to the DMI, the magnetic moments are slightly canted, forming a nonzero magnetization along e_l , in agreement with experiments [25,27]. The symmetry of the local environment also suggests that ρ_{AHE} measured in the (0001) plane transforms in the same way as the out-of-plane component of magnetization m_z and the component of the Néel vector n_j along the easy axis. Thus, we

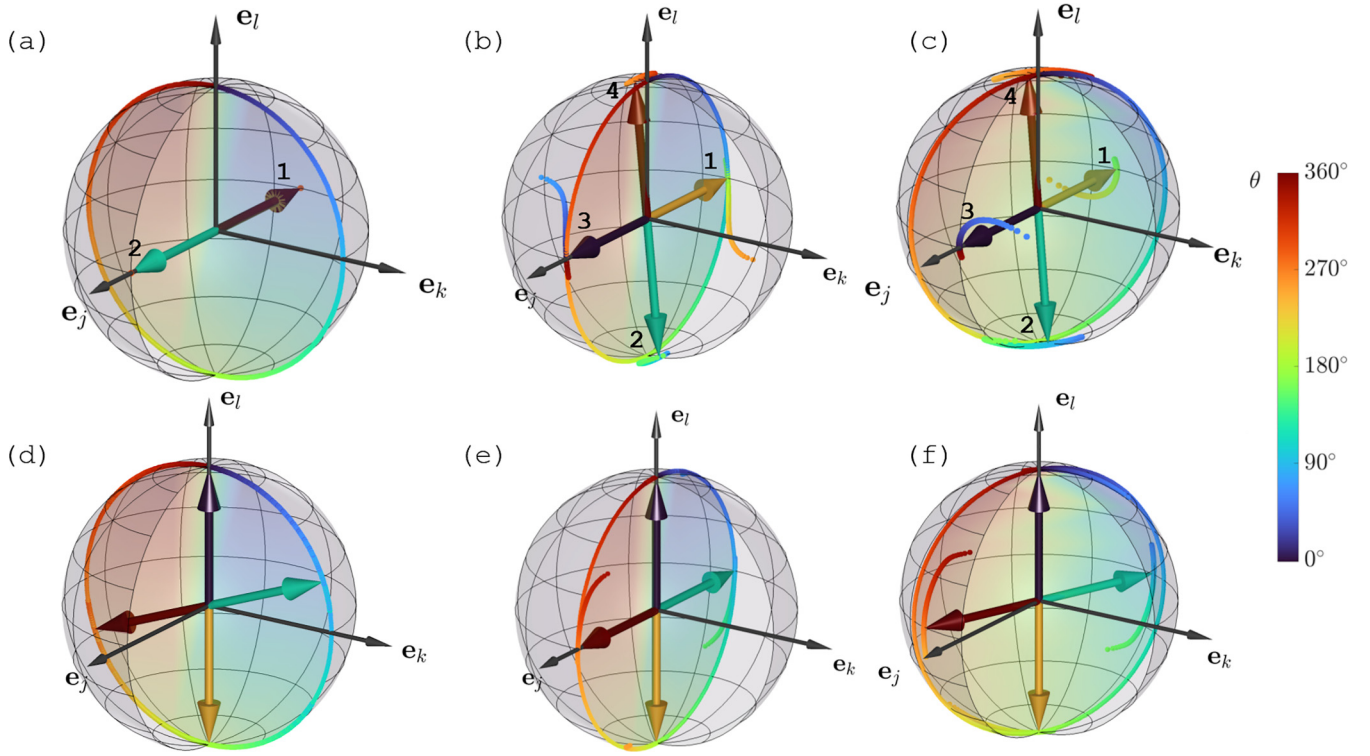


FIG. 3. Calculated states of \mathbf{n} (a)–(c) and \mathbf{m} (d)–(f), when \mathbf{H} is rotated in different planes. The frame $\mathbf{e}_j, \mathbf{e}_k, \mathbf{e}_l$ depends on the variant considered [Fig. 1(a)]. For example, for variant (ii), (a), (d) is when \mathbf{H} is rotated in the $(\bar{1}\bar{1}20)$ plane [Fig. 2(b)], (b), (e) in the $(\bar{1}\bar{1}00)$ plane [Fig. 2(e)], and (c), (f) in any other plane [Figs. 2(a), 2(c), 2(d), and 2(f)]. The disk outline describes the \mathbf{H} trajectory. The arrows describe the orientations of \mathbf{n} and \mathbf{m} , in panels (a)–(c) and (d)–(f), respectively, for selected \mathbf{H} orientations. The color code indicates the correspondence between the orientations of \mathbf{n} (\mathbf{m}) and \mathbf{H} . Discontinuous traces are linked to transient states. The numbers (1,2) and (1,2,3,4) correspond to those in Fig. 2.

assume that the transverse resistivity has two contributions, $\rho_{\text{AHE}}/\rho_{\text{AHE,max}} = \alpha \cos(\widehat{\mathbf{n}}, \mathbf{e}_j) + \beta \cos(\widehat{\mathbf{m}}, \mathbf{z})$, where α and β are phenomenological constants, $(\widehat{\mathbf{n}}, \mathbf{e}_j)$ is the angle between \mathbf{n} and $[\bar{1}\bar{1}20]$, and $(\widehat{\mathbf{m}}, \mathbf{z})$ is the angle between \mathbf{m} and $[0001]$. The best match with the experimental data in Fig. 2 is obtained for $\alpha = 0.8$ and $\beta = 0.6$. The individual contributions from \mathbf{n} and \mathbf{m} to ρ_{AHE} are shown in the SM (Fig. S15). In the approximation of strong exchange coupling between magnetic sublattices, \mathbf{m} is a slave variable determined by \mathbf{n} . Therefore, $\rho_{\text{AHE}}(\mathbf{H})$ and $\mathbf{n}(\mathbf{H})$ are in one-to-one correspondence, which allows us to reconstruct the magnetic structure based on the Hall measurements for a single variant [Fig. 1(a)].

Our calculations revealed three types of angular dependencies $\mathbf{n}(\mathbf{H})$ at field values greater than the out-of-plane coercive field. We first consider the specific case when \mathbf{H} is rotated in the plane perpendicular to \mathbf{e}_j [Fig. 3(a)], i.e., the $(\bar{1}\bar{1}20)$ plane for variant type (ii) [Fig. 2(b)]. Two states with opposite orientation of \mathbf{n} , along $\pm \mathbf{e}_j$, are nondegenerate. \mathbf{H} rotation can only induce a steplike 180° switching. In this case, the slopes $(dn_j/d\theta)_{90^\circ}$ and $(d\rho_{\text{AHE}}/d\theta)_{90^\circ}$ go to infinity and the θ dependence near $\theta = 90^\circ$ is steplike, in agreement with the experimental findings [Fig. 2(b)]. The stability of these states is determined mainly by the magnetic anisotropy resulting in a wide hysteresis and large coercivity in the θ scans. We next consider the case when \mathbf{H} has a nonzero projection on \mathbf{e}_j [Fig. 3(b)], i.e., when it is rotated in the $(\bar{1}\bar{1}00)$ plane for variant type (ii) [Fig. 2(e)]. This can induce a spin-flop transition leading to the trapping of \mathbf{n} in one of two metastable states

close to out of plane: $\mathbf{n} \parallel \pm \mathbf{e}_l$. In this case, \mathbf{n} hops between four states during \mathbf{H} rotation: $\mathbf{n} \parallel \mathbf{e}_j \Rightarrow \mathbf{e}_l \Rightarrow -\mathbf{e}_j \Rightarrow -\mathbf{e}_l$. The stability of the additional, “out-of-plane” states is determined by the DMI, which sets the hard magnetic axes along $\mathbf{e}_j \pm \mathbf{e}_l$ and $\mathbf{e}_k \perp \mathbf{e}_j, \mathbf{e}_l$. Thus, the energy trap is maximal when \mathbf{H} is rotated in the $(\mathbf{e}_j, \mathbf{e}_l)$ plane, i.e., $(\bar{1}\bar{1}00)$ for variant type (ii). In this case, the stability range of the out-of-plane states is large, which leads to the large hysteresis and strong coercivity [Fig. 2(e)]. Moreover, the slope $(dn_j/d\theta)_{90^\circ}$ is negative and $(d\rho_{\text{AHE}}/d\theta)_{90^\circ}$ can be either negative or positive depending on the ratio α/β [Fig. 2(e) and Fig. S15]. We finally consider all other intermediate cases [Figs. 3(c), 2(a), 2(c), 2(d), and 2(f)]. From the maximum when \mathbf{H} is rotated in the $(\mathbf{e}_j, \mathbf{e}_l)$ plane, the stability range of the out-of-plane state decreases for other planes of rotation. As a result, the slope $(dn_j/d\theta)_{90^\circ}$ evolves continuously from a maximum negative value to large positive values for $\mathbf{H} \perp \mathbf{e}_j$, where the out-of-plane states are unstable. This also results in a variation of the hysteresis width, which is pronounced in two limiting cases and almost disappears for intermediate cases.

We note that the model also reproduces $\rho_{\text{AHE}}(\mathbf{H})$ [Fig. 1(a) and Fig. S2(b)]. In addition, we would like to point out that the initial model of altermagnetism in Mn_5Si_3 was deduced from the four magnetically ordered Mn2 atoms, which are at Wyckoff positions that are conducive to d -wave altermagnetism with the $d_{x^2-y^2}$ symmetry [25]. With this symmetry, \mathbf{n} pointing in plane along an axis of high symmetry, e.g., $[2\bar{1}\bar{1}0]$ and its two equivalents, was forbidden as it did not allow

an out-of-plane Hall vector. The model returned a ground state in which \mathbf{n} was along $[2\bar{2}01]$, then used in Refs. [14] and [26]. Our refined model showed that the symmetry of the altermagnetic phase of Mn_5Si_3 is actually lower. Here, the \mathbf{n} was derived from energy minimization from the non-magnetic phase, considering the local environment of the Mn2 atoms. The environment corresponding to the crystallographic positions reproduces the $d_{x^2-y^2}$ symmetry of the initial model. Convergence of energy minimization requires inhomogeneous displacements of Si and Mn1 atoms, which reduces the symmetry from a magnetically unordered but already altermagnetic phase down to the monoclinic phase. In this phase of lower symmetry, \mathbf{n} pointing in plane along an axis of high symmetry allows an out-of-plane Hall vector. Our model thus returned a ground state in which \mathbf{n} connects the two unordered Mn atoms in the basal plane. For variant types (i), (ii), and (iii), \mathbf{n} is along $[2\bar{1}\bar{1}0]$, $[\bar{1}\bar{1}20]$, and $[\bar{1}2\bar{1}0]$, respectively. We note that, compared to our epitaxial thin films, the magnetic phase of Mn_5Si_3 in bulk and polycrystals is not altermagnetic and displays a different orientation of \mathbf{n} [44,45].

Based on the relationship between the variants [Fig. 1(a)], the features corresponding to variant type (ii) (e.g., the marked hysteresis for $\phi = 30^\circ$) are rotated by 120° in plane for type (iii) variant and -120° in plane for type (i). Consequently, we can conclude that the weak hysteresis observed in Figs. 2(d) and 2(f) for $\phi = 90$ and 150° highlight contributions from minority variants of types (i) and (iii), respectively [Fig. 1(a)]. We assume that local defects can lift the degeneracy between the variants and locally favor one over the other. Experiments on another such Hall cross, located elsewhere in the sample and oriented in the same way, enabled us to identify a region where the altermagnetic variant type (iii) [Fig. 1(a)] was in the majority (Fig. S4). This conclusion could be drawn because the H -related anisotropy pattern (set of six angular dependencies) was shifted by $+120^\circ$ compared to the pattern we observed for variant type (ii) (Fig. 2). We can also deduce that patterning does not favor a specific variant, for example through strain.

Ultimately, when all variants are equally populated, i.e., for a mesoscopic $10\text{-}\mu\text{m}$ -wide Hall cross, the set of data when \mathbf{H} is rotated in the $(\bar{2}110)$ plane and its two equivalents superimpose [Fig. 4(a)] [27]. In fact, for such a mesa, the fingerprint of variant (i), (ii), and (iii), i.e., the marked hysteresis around $\theta = 90^\circ$ and 270° , occurs when \mathbf{H} is rotated in the $(\bar{2}110)$, $(\bar{1}\bar{1}20)$, and $(\bar{1}2\bar{1}0)$ planes, respectively (Figs. S18–S20). Because the fingerprints superimpose, and because the current is always along $(0\bar{1}\bar{1}0)$, i.e., oriented differently for all three variants in the mesa, we can confirm [27] that the anisotropic pattern of the AHE relates to the crystal plane in which the field rotates, rather than to the crystal axis along which the current channel is oriented. We note that current-related effects may occur for large current densities, in which anisotropic spin polarization can take place [46]. The mesoscopic configuration is equivalent to averaging over the signals obtained for a given variant [Fig. 4(b)]. Similar results were obtained for data sets when \mathbf{H} is rotated in the $(0\bar{1}\bar{1}0)$ plane and its two equivalents [Figs. 4(c) and 4(d)]. We note that the use of larger H of 4 and 7 T causes a reduction of the hysteresis in the angular scan [27] (Figs. S16 and S17). The stable and metastable states, which are key to

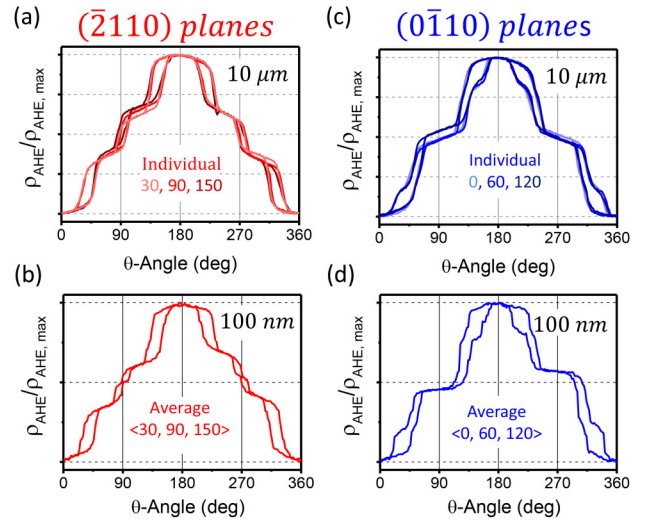


FIG. 4. (a),(c) Superposition of the individual Hall signals, when \mathbf{H} is rotated in the $(\bar{2}110)$ plane and its two equivalents $[(0\bar{1}\bar{1}0)$, respectively], measured for a $10\text{-}\mu\text{m}$ -wide Hall bar containing all variants [Fig. 1(a)]. (b), (d) Averaged Hall response over all signals obtained in Figs. 2(b), 2(d), and 2(f) [(a), (c), (e), respectively], when \mathbf{H} is rotated in the $(\bar{2}110)$ plane and equivalents $[(0\bar{1}\bar{1}0)$, respectively], i.e., for $\phi = 0^\circ, 60^\circ, 120^\circ$ ($30^\circ, 90^\circ, 150^\circ$, respectively), for a 100-nm -wide Hall cross containing mainly one variant.

the deduction of the variant, and the conclusions of our work are unaffected.

In conclusion, the main contribution of this Letter is the experimental demonstration of the, so far, presumed altermagnetic arrangement of magnetic moments with respect to crystal symmetries in thin films of Mn_5Si_3 , via identification of variants, i.e., the three options for the checkerboard distribution of the magnetic Mn atoms [Fig. 1(a)]. Our experimental data revealed the symmetries of the system, at the nanoscale, through anisotropy of the AHE for nanometric devices. They elevate Mn_5Si_3 from a candidate to a proven altermagnet. The magnetic moment–crystal axes arrangement was reshuffled via field-driven variation of the Néel vector, with a field applied at several angles. These findings were corroborated by a refined theoretical model accounting for the local environment of the magnetic sublattices. Corroborating the model and the experiments revealed the ground state, as well as the trajectories of the Néel vector and net magnetization due to DMI-induced canting. This information was inaccessible until now, because variants were not isolated. Our study therefore opens up prospects for a wide range of further fundamental research and practical applications in altermagnetism, where detecting and controlling altermagnetism is critical. We also wish to open the conversation on the implications of variants. A magnetic variant differs from a magnetic domain, in that a single variant can contain two magnetic domains of opposite direction. Magnetic variants, therefore, bring an additional degree of freedom to the system. How to exploit this degree of freedom, how to control it, what is the ground state between two variants, and how variants evolve across the Néel temperature are open questions. For example, a magnetic field is not expected to directly modify nonmagnetic atoms, and the process by which, e.g., strain, one

variant can be more densely populated than the other is an open challenge.

We thank G. Atcheson for critical reading of the manuscript, and D. Gusakova and C. Thevenard for fruitful discussions. This work was supported by the French National Research Agency (ANR) and the Deutsche Forschungsgemeinschaft (DFG) (Project MATHEEIAS, Grant No. ANR-20-CE92-0049-01/DFG-445976410, and Project PEPR SPIN, Grant No. ANR-22-EXSP-0007). H.R., E.S., S.T.B.G., and A.T. were supported by the DFG-GACR Grant No. 490730630. J.R. acknowledges MINECO for the Margaritas

Salas program. D.K. acknowledges the Academy of Sciences of the Czech Republic (Project No. LQ100102201). O.G. and J.S. acknowledge funding by DFG Grant No. TRR 288-422213477 (Projects No. A09 and No. A12) and TRR 173-268565370 (Projects No. A03, No. A11, and No. B15). A.B., E.S., D.K., L.S., T.J. acknowledge the Ministry of Education, Youth and Sports of the Czech Republic through the OP JAK call Excellent Research (TERAFIT Project No. CZ.02.01.01/00/22_008/0004594). T.J. acknowledges support by the Ministry of Education of the Czech Republic CZ.02.01.01/00/22008/0004594 and, ERC Advanced Grant No. 101095925.

-
- [1] L. Šmejkal, J. Sinova, and T. Jungwirth, Emerging research landscape of altermagnetism, *Phys. Rev. X* **12**, 040501 (2022).
- [2] L. Šmejkal, J. Sinova, and T. Jungwirth, Beyond conventional ferromagnetism and antiferromagnetism: A phase with nonrelativistic spin and crystal rotation symmetry, *Phys. Rev. X* **12**, 031042 (2022).
- [3] L. Šmejkal, R. González-Hernández, T. Jungwirth, and J. Sinova, Crystal time-reversal symmetry breaking and spontaneous Hall effect in collinear antiferromagnets, *Sci. Adv.* **6**, eaaz8809 (2020).
- [4] H. Yan, X. Zhou, P. Qin, and Z. Liu, Review on spin-split antiferromagnetic spintronics, *Appl. Phys. Lett.* **124**, 030503 (2024).
- [5] L.-D. Yuan, Z. Wang, J.-W. Luo, E. I. Rashba, and A. Zunger, Giant momentum-dependent spin splitting in centrosymmetric low-Z antiferromagnets, *Phys. Rev. B* **102**, 014422 (2020).
- [6] S. Hayami, Y. Yanagi, and H. Kusunose, Momentum-dependent spin splitting by collinear antiferromagnetic ordering, *J. Phys. Soc. Jpn.* **88**, 123702 (2019).
- [7] V. Baltz, A. Manchon, M. Tsoi, T. Moriyama, T. Ono, and Y. Tserkovnyak, Antiferromagnetic spintronics, *Rev. Mod. Phys.* **90**, 015005 (2018).
- [8] T. Jungwirth, X. Marti, P. Wadley, and J. Wunderlich, Antiferromagnetic spintronics, *Nat. Nanotechnol.* **11**, 231 (2016).
- [9] Z. Feng *et al.*, An anomalous Hall effect in altermagnetic ruthenium dioxide, *Nat. Electron.* **5**, 735 (2022).
- [10] T. Tschirner *et al.*, Saturation of the anomalous Hall effect at high magnetic fields in altermagnetic RuO₂, *APL Mater.* **11**, 101103 (2023).
- [11] X. Zhou, W. Feng, R. W. Zhang, L. Šmejkal, J. Sinova, Y. Mokrousov, and Y. Yao, Crystal thermal transport in altermagnetic RuO₂, *Phys. Rev. Lett.* **132**, 056701 (2024).
- [12] A. Badura *et al.*, Observation of the anomalous Nernst effect in altermagnetic candidate Mn₅Si₃, [arXiv:2403.12929](https://arxiv.org/abs/2403.12929).
- [13] L. Han, X. Fu, W. He, Y. Zhu, J. Dai, and W. Yang, Observation of non-volatile anomalous Nernst effect in altermagnet with collinear Néel vector, [arXiv:2403.13427](https://arxiv.org/abs/2403.13427).
- [14] J. K. Dai *et al.*, Thermal-modulation spin-orbit torque for 180° Néel vector switching, *Phys. Rev. Mater.* **8**, 074406 (2024).
- [15] M. Naka, S. Hayami, H. Kusunose, Y. Yanagi, Y. Motome, and H. Seo, Spin current generation in organic antiferromagnets, *Nat. Commun.* **10**, 4305 (2019).
- [16] H. Y. Ma, M. Hu, N. Li, J. Liu, W. Yao, J. F. Jiá, and J. Liu, Multifunctional antiferromagnetic materials with giant piezomagnetism and noncollinear spin current, *Nat. Commun.* **12**, 2846 (2021).
- [17] A. Bose *et al.*, Tilted spin current generated by the collinear antiferromagnet ruthenium dioxide, *Nat. Electron.* **5**, 267 (2022).
- [18] H. Bai *et al.*, Observation of spin splitting torque in a collinear antiferromagnet RuO₂, *Phys. Rev. Lett.* **128**, 197202 (2022).
- [19] S. Karube, T. Tanaka, D. Sugawara, N. Kadoguchi, M. Kohda, and J. Nitta, Observation of spin-splitter torque in collinear antiferromagnetic RuO₂, *Phys. Rev. Lett.* **129**, 137201 (2022).
- [20] B. Chi, L. Jiang, Y. Zhu, G. Yu, C. Wan, J. Zhang, and X. Han, Crystal-facet-oriented altermagnets for detecting ferromagnetic and antiferromagnetic states by giant tunneling magnetoresistance, *Phys. Rev. Appl.* **21**, 034038 (2024).
- [21] R. D. Gonzalez Betancourt *et al.*, Spontaneous anomalous Hall effect arising from an unconventional compensated magnetic phase in a semiconductor, *Phys. Rev. Lett.* **130**, 036702 (2023).
- [22] L. Šmejkal, A. B. Hellenes, R. González-Hernández, J. Sinova, and T. Jungwirth, Giant and tunneling magnetoresistance in unconventional collinear antiferromagnets with nonrelativistic spin-momentum coupling, *Phys. Rev. X* **12**, 011028 (2022).
- [23] S. Xu *et al.*, Spin-flop magnetoresistance in a collinear antiferromagnetic tunnel junction, [arXiv:2311.02458](https://arxiv.org/abs/2311.02458).
- [24] K. P. Kluczyk *et al.*, Coexistence of anomalous Hall effect and weak net magnetization in collinear antiferromagnet MnTe, *Phys. Rev. B* **110**, 155201 (2024).
- [25] H. Reichlova *et al.*, Observation of a spontaneous anomalous Hall response in the Mn₅Si₃ d-wave altermagnet candidate, *Nat. Commun.* **15**, 4961 (2024).
- [26] L. Han *et al.*, Electrical 180° switching of Néel vector in spin-splitting antiferromagnet, *Sci. Adv.* **10**, eadn0479 (2024).
- [27] M. Leiviskä *et al.*, Anisotropy of the anomalous Hall effect in the altermagnet candidate Mn₅Si₃ films, *Phys. Rev. B* **109**, 224430 (2024).
- [28] A. Badura *et al.*, Even-in-magnetic-field part of transverse resistivity as a probe of magnetic order, [arXiv:2311.14498](https://arxiv.org/abs/2311.14498).
- [29] I. Kounta *et al.*, Competitive actions of MnSi in the epitaxial growth of Mn₅Si₃ thin films on Si(111), *Phys. Rev. Mater.* **7**, 024416 (2023).
- [30] R. D. Gonzalez Betancourt *et al.*, Anisotropic magnetoresistance in altermagnetic MnTe, *npj Spintronics* **2**, 45 (2024).
- [31] S. Reimers *et al.*, Direct observation of altermagnetic band splitting in CrSb thin films, *Nat. Commun.* **15**, 2116 (2024).

- [32] T. Osumi, S. Souma, T. Aoyama, K. Yamauchi, A. Honma, K. Nakayama, T. Takahashi, K. Ohgushi, and T. Sato, Observation of a giant band splitting in altermagnetic MnTe, *Phys. Rev. B* **109**, 115102 (2024).
- [33] J. Krempaský *et al.*, Altermagnetic lifting of Kramers spin degeneracy, *Nature (London)* **626**, 517 (2024).
- [34] O. Fedchenko *et al.*, Observation of time-reversal symmetry breaking in the band structure of altermagnetic RuO₂, *Sci. Adv.* **10**, eadj4883 (2024).
- [35] S. Lee *et al.*, Broken kramers degeneracy in altermagnetic MnTe, *Phys. Rev. Lett.* **132**, 036702 (2024).
- [36] R. M. Sattigeri, G. Cuono, and C. Autieri, Altermagnetic surface states: Towards the observation and utilization of altermagnetism in thin films, interfaces and topological materials, *Nanoscale* **15**, 16998 (2023).
- [37] C. Li *et al.*, Topological weyl altermagnetism in CrSb, [arXiv:2405.14777](https://arxiv.org/abs/2405.14777).
- [38] J. Ding *et al.*, Large band-splitting in g-wave type altermagnet CrSb, *Phys. Rev. Lett.* **133**, 206401 (2024).
- [39] A. Hariki, T. Okauchi, Y. Takahashi, and J. Kuneš, Determination of the Neel vector in rutile altermagnets through x-ray magnetic circular dichroism: The case of MnF₂, *Phys. Rev. B* **110**, L100402 (2024).
- [40] G. Yang *et al.*, Three-dimensional mapping and electronic origin of large altermagnetic splitting near Fermi level in CrSb, [arXiv:2405.12575](https://arxiv.org/abs/2405.12575).
- [41] O. J. Amin *et al.*, Nanoscale imaging and control of altermagnetism in MnTe, *Nature* **636**, 348 (2024).
- [42] See Supplemental Material at <http://link.aps.org/supplemental/10.1103/PhysRevB.110.L220411> for more information on the experiments and the theoretical model.
- [43] O. Gomonay, V. P. Kravchuk, R. Jaeschke-Ubiergo, K. V. Yershov, T. Jungwirth, L. Šmejkal, J. van den Brink, and J. Sinova, Structure, control, and dynamics of altermagnetic textures, *npj Spintronics* **2**, 35 (2024).
- [44] C. Sürgers, G. Fischer, P. Winkel, and H. V. Löhneysen, Large topological Hall effect in the non-collinear phase of an antiferromagnet, *Nat. Commun.* **5**, 3400 (2014).
- [45] M. Gottschilch, O. Gourdon, J. Persson, C. De La Cruz, V. Petricek, and T. Brueckel, Study of the antiferromagnetism of Mn₅Si₃: An inverse magnetocaloric effect material, *J. Mater. Chem.* **22**, 15275 (2012).
- [46] R. González-Hernández, L. Šmejkal, K. Výborný, Y. Yahagi, J. Sinova, T. Jungwirth, and J. Železný, Efficient electrical spin splitter based on nonrelativistic collinear antiferromagnetism, *Phys. Rev. Lett.* **126**, 127701 (2021).